# A Normalized Diagram for Compare Densities in Additive Manufacturing of Iron-Silicon Magnetic Alloys

Abilo Andrés Velásquez Salazar, Alejandro Ospina Vargas, Yuyang Li, Noureddine Fenineche, Jêrome Favergeon, Thierry Baffie, Meher Zaied, Salima Bouvier

# A Normalized Diagram for Compare Densities in Additive Manufacturing of Iron-Silicon Magnetic Alloys

Abilo Andrés Velásquez Salazar[1], Yuyang Li[1], Alejandro Ospina Vargas[1], Meher Zaied[2], Noureddine Fenineche[2], Jêrome Favergeon[1], Thierry Baffie[3], Salima Bouvier[1]
[1]Université de technologie de Compiègne, Laboratory Roberval, Compiègne, France
[2] ICB LERMPS ICB UMR 6303, CNRS, Univ. Bourgogne Franche-Comté, UTBM, F-90010 Belfort, France
[3]Univ. Grenoble Alpes, CEA, LITEN, F-38000 Grenoble, France
abilo-andres.velasquez-salazar@utc.fr

***Abstract***

*This article explores additive manufacturing of magnetic materials via Selective Laser Melting (SLM), integrating insights from prior studies. The principal goal is compare densities for* different *studies about magnetics materials (FeSi alloys) using a normalized energy diagram. This diagram is a convenient tool that help in the identification of different density regions: incomplete melting, bubble formation, insufficient power for melting, and finally, optimal conditions. Further, we examine density variations in Fe-3%Si, Fe-6.7%Si, and Fe-6.9%Si alloys, highlighting the impact of silicon content on final density. This comparative analysis provides insights into the intricate relationship between process parameters and additive manufacturing of magnetic materials through SLM. This study contributes to understanding dynamic interactions shaping magnetic material density. By optimizing process parameters based on density considerations, microstructure tailoring becomes possible, influencing the final magnetics properties (magnetic saturation, coercive field and so on). Thus, the implications of an optimal control of densities is an important step for a further studies about rapid prototyping of electric machines by Additive Manufacturing (AM)M*

***Keywords: Additive Manufacturing, Selective Laser Melting (SLM), Fe-Si alloys and Normalized process maps.***

## I. INTRODUCTION

For more than a century, FeSi alloys have been used in the laminated cores of electrical machines [10][11]. Consequently, there are numerous studies about the production methods, the suitable chemical compositions, the interaction between these processes, the micro-structure obtained, and the final properties of these alloys. However, the recent introduction of AM opened new ways to design and produce electric machines, and, like in the case of classical production methods, these new processes need a deep understanding of the interaction between manufacturing, microstructure, and final physical properties. Recently, some studies have focused on the Selective Laser Melting (SLM) technique as a suitable process that can produce this kind of ferromagnetic alloys. Due to the thermal nature of the SLM (rapid cooling), it allows for the adjustment of micro-structural parameters influencing final mechanical and magnetic properties. Consequently, due to the production strategy and supplied power, there is an impact on the final density of the material [19]. This density is related to magnetic and electrical parameters affecting losses due to eddy currents and saturation magnetization.

Understanding and controlling the density of additively manufactured magnetic materials using Selective Laser Melting (SLM) is critical for advancing energy-efficient electrical systems. This research integrates insights from Moda et al.[14], Ion et al.[8], Thomas et al.[18], and Zaied et al.[19] to address density variation concerning applied energies. Beyond this, a change is introduced in the way normalized diagrams are constructed. This change involves using the width of the melt pool, theoretically calculated by Mendez *et.al* [12], instead of the laser spot radius. As a result, the data appears more scattered in the diagram, allowing for better stratification with respect to density.

This study holds broader implications for improving the efficiency of electrical machines, aligning with ongoing efforts to reduce energy consumption and enhance overall system efficiency, as highlighted by Krings[11]. The non-linear density behavior observed in additive manufacturing parallels challenges outlined by Krings in minimizing losses. Thus, it is observed that density is low for both low and high energy density configurations, and at some intermediate point, the density approaches that of the solid bulk material. Gaining control over density variations is pivotal, not just for producing magnetic materials but also for designing high-efficiency electrical machines that play a key role in global energy conservation.

In addition to the proposals and methodologies mentioned, this research aims to contribute to the understanding of how the density of magnetic materials can be optimized during the additive manufacturing process. By exploring the construction of normalized process maps and considering the influence of excess energy, this study adapts to the nonlinear behavior of density concerning applied energies. The visualization of the relationship between production parameters and resulting density under different energy levels becomes a crucial resource for identifying configurations that lead to density maxima.

Throughout this article, we will examine experimental procedures, obtained results, and conclusions derived from this applied methodology. Emphasis will be placed on identifying optimal configurations that enable achieving maximum densities, considering variations in applied energies in the additive manufacturing of magnetic materials via SLM.

## II. Normalized Process Maps for Additive Layer Manufacture

In the pursuit of optimizing parameters for additive manufacturing, inspiration is drawn from the work proposed by Ion et al. and Thomas et al., specifically their methodology for constructing normalized process maps. This approach, though initially developed across various additive manufacturing technologies and not specifically focused on magnetic materials, provides a solid foundation.

### A. *Construction of Normalized Process Maps*

The process begins with the consideration of normalized volumetric energy (1), expressed as:

$$E^* = \frac{P^*}{v^* h^* l^*} \quad (1)$$

Where, $(*)$ indicates normalized parameters:

1) *Dimensionless power*:
$$P^* = \frac{AP}{r_b \lambda \Delta T}$$
with $A$ as the surface absorptivity of the alloy, $P$ the laser power, $r_b$ the radius of the laser beam, $\lambda$ the thermal conductivity, and $\Delta T = T_m - T_0$ as the difference between the melting temperature, $T_m$, and the initial substrate temperature, $T_0$.
2) *Dimensionless scanning velocity*: $v^* = v r_b/\alpha$ with $v$ as the scanning velocity, and $\alpha = \lambda/(\rho c_p)$ as the thermal diffusivity, defined as the conductivity divided by the density $\rho$ and the specific heat $c_p$.
3) *Dimensionless hatch distance*: $h^* = h/r_b$ with $h$ as the distance between scan paths.
4) *Dimensionless layer thickness*: $l^* = l/(2r_b)$ with $l$ as the layer thickness.

In the subsequent analysis, the normalized diagram (Fig. 1) is applied to the literature review presented in Table 2 and completed with Tab. 1 and Tab. 2 . The diagram is constructed using the equation (1), where x=P^*/(v^* l^*) and y=1/h^*, as suggested in the literature. The positioning of data points around x≈4 and y≈1 indicates that researchers aim for a hatch distance close to the laser spot radius and a location that complements the normalized energy to be several times the energy required to melt the entire material scanned. This high energy does not necessarily imply low process efficiency but rather reflects the use of absorbance near 30%, a situation subject to discussion. Additionally, each consulted author reported the effects of modifying parameters by increasing or decreasing the normalized energy, as illustrated in the mentioned diagram. This diagram captures the occurrence of solidification fractures and porosity, providing valuable insights into the impact of construction parameters on material properties.

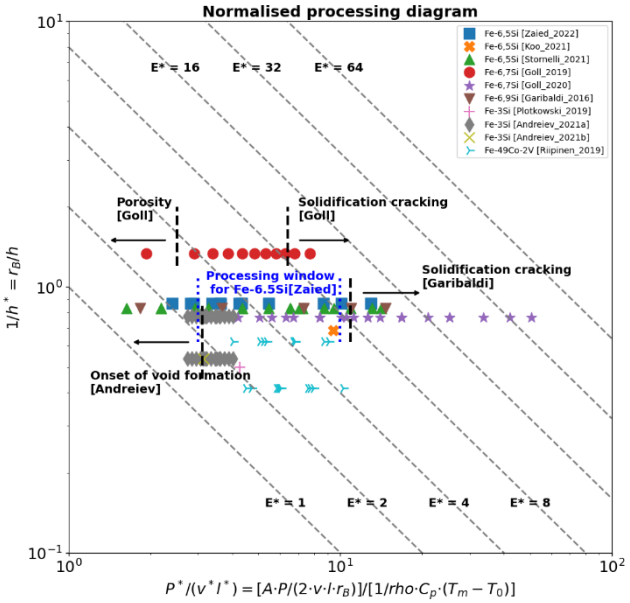

Figure 1: Standardized process diagram of soft magnetic materials.

These tables (1 and 2 ) present comprehensive sources for both process parameter data and thermodynamic material data. The process parameter data table includes information on laser power, scanning velocity, hatch distance, and layer thickness, while the thermodynamic material data table encompasses key properties required for the additive manufacturing of magnetic materials.

This diagram offers valuable insights into how variations in materials and process parameters impact the normalized energy. The scaling considerations become particularly evident when comparing different materials under the same process conditions or the same material under varying conditions. Such visualizations aid in identifying trends and outliers, guiding the selection of optimal parameters for achieving desired material properties.

In the subsequent sections, we delve into the specifics of our methodology and present our findings in the context of additive manufacturing of magnetic materials via Selective Laser Melting.

TABLE 1: Summary of additive manufacturing process parameters for soft magnetic materials presented in the literature

| Article | Alloy | Procedure | $P[W]$ | $v[m.s^{-1}]$ | $h[\mu m]$ | $l[\mu m]$ | $r_b[\mu m]$ | $T_0[^\circ C]$ |
|---|---|---|---|---|---|---|---|---|
| Zaied 2022[?] | Fe-6,5Si | L-PBF | 60-90 | 0.15-0.5 | 60 | 30 | 52 | 240 |
| Koo 2021[9] | Fe-6,5Si | SS-SLM | 90 | 0.2 | 80 | 25 | 55 | 23 |
| Stornelli 2021[17] | Fe-6,5Si | L-PBF | 75-325 | 0.5 - 1 | 60 | 30 | 50 | 200 |
| Goll 2019[6] | Fe-6,7Si | L-PBF | 100-400 | 0.5 | 60 | 50 | 80 | 400 |
| Goll 2020[7] | Fe-6,7Si | L-PBF | 100-300 | 0.1 - 0.5 | 60 | 50 | 46 | 400 |
| Garibaldi 2016[3] | Fe-6,9Si | SLM | 70 | 0.125 - 1 | 60 | 25 | / | 200 |
| Garibaldi 2018a[4] | Fe-6,9Si | SLM | 70 | 0.125 - 0.5 | 60 | 25 | / | 200 |
| Garibaldi 2018b[5] | Fe-6,9Si | SLM | 70 | 0.5 | 60 | 25 | / | 200 |
| Plotkowski 2019[15] | Fe-3Si | L-PBF | 200 | 0.6818 | 100 | 50 | / | / |
| Andreiev 2021a[1] | Fe-3Si | L-PBF | 220-280 | 0.65 - 0.75 | 90 - 130 | 50 | 70 | 200 |
| Andreiev 2021b[2] | Fe-3Si | L-PBF | 235 | 0.7 | 130 | 50 | 70 | 200 |
| Riipinen 2019[16] | Fe-49Co-2V | L-PBF | 150-225 | 0.575 - 0.975 | 80 - 120 | 25 | / | 200 |

TABLE 2: Thermo-physical properties of Fe-Si material

| Property | Quantity | Unity | References |
|---|---|---|---|
| Solidification temperature | 1700 | $K$ | [13] |
| Liquefaction temperature | 1773 | $K$ | [13] |
| Theoretical density ($\rho$) | 7.5 | $g/cm^3$ | |
| Thermal conductivity ($\lambda$) | 45 | $W.m^{-1}.K^{-1}$ | [15] |
| Thermal capacity of the material ($c_p$) | 470 | $J/kg.K$ | [15] |

TABLE 3: Thermo-physical properties of Fe-49Co-2V wt(%) material

| Property | Quantity | Unity | References |
|---|---|---|---|
| Solidification temperature | 1721.55 | $K$ | JMatPro |
| Liquefaction temperature | 1733.99 | $K$ | JMatPro |
| Theoretical density ($\rho$) | 8.28($25^\circ C$) | $g/cm^3$ | JMatPro |
| Thermal conductivity ($\lambda$) | 20.85($25^\circ C$) | $W.m^{-1}.K^{-1}$ | JMatPro |
| Thermal capacity of the material ($c_p$) | 490($25^\circ C$) | $J/kg.K$ | JMatPro |

### B. *Parameter Scaling New Consideration*

Now, we have adopted a modification suggested by Moda *et al.*., where the laser radius, $r_b$, is replaced by the estimated width of the melt pool, denoted as $2R$. This adjustment is justified as it aligns with the work of Moda et al., who employed the solution proposed by Mendez et al.[12] for the Rosenthal equation to obtain melt pool dimensions. This modification becomes crucial due to the diverse nature of materials and the varying energy requirements for phenomena such as bubble generation or partial melting of metallic powder including cracking formation. The revised normalization allows for a comparative analysis to identify optimal parameters based on the desired final material density. For simplicity, we will describe only the basic calculations needed for this change like Rykalin number, $R_y$ (3), characteristic length, $l_{R_y}$ (4), and half-width and penetration of the melted zone, $R$ (5).

$$R_y = \frac{Pv}{4\pi\lambda\alpha\Delta T_m} \tag{3}$$

$$l_{R_y} = \frac{2\alpha}{v} \tag{4}$$

$$R \approx l_{R_y} R_y \left[1 + \left(\frac{2}{eR_y}\right)^{\frac{\beta}{2}}\right]^{\frac{1}{\beta}} \tag{5}$$

with $\beta = -1.7312$

Scaled normalized parameters, such as energy, power, scanning velocity, hatch distance, and layer thickness, to dimensions like the width and depth of the melt pool rather than the size of the laser spot is advisable. The size of the melt pool is intricately linked to these values, and the size of the laser spot does not proportionally represent the shape of this pool.

## III. Results and Discussion

### A. *Density Variation in Fe-6.5%Si Alloy*

In this investigation of the Fe-6.5%Si alloy, the data from three authors [19], [9], [17] were analyzed. Fig. 2 illustrates the density variation with respect to key process parameters, providing a comprehensive view of how different conditions influence the final density. It's important to note that this figure is scaled to the width and depth of the melt pool, calculated using the method proposed by Méndez *et al.* and reported by Moda *et al.* on SLM. The Méndez method, derived from the Rosenthal function, defines the shape of the melt pool based on the region where the temperature is greater than or equal to the alloy's liquefaction temperature. For the aforementioned reason, this new diagram disperses information more effectively, being more sensitive to the thermal properties of the material and its density. Therefore, it is necessary to narrow the visualization window to better appreciate how these diagrams are segmented. It is also worth mentioning that this thorough exploration is conducted because the authors are producing materials increasingly closer to the optimal points.

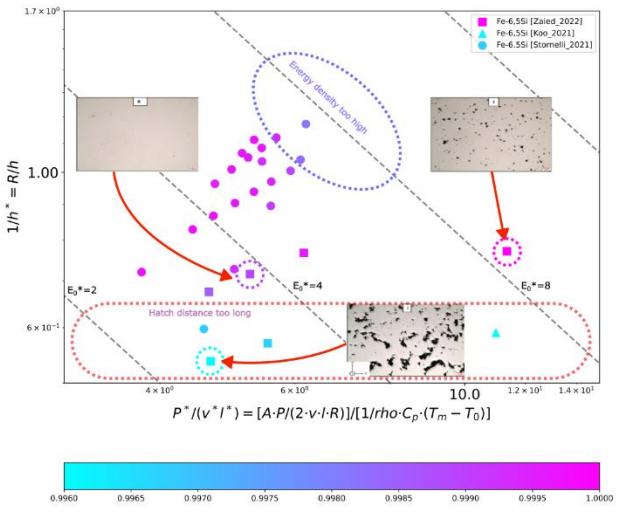


Figure 2: Standardized process diagram for Fe-6.5Si. The micrographs were taken on the highlighted samples and represent the causes of the density decrease. The color on the marker represents the proportion of density it maintains with respect to the theoretical

The normalized energy diagram for the Fe-6.5%Si alloy reveals four distinct regions, each providing valuable insights into the additive manufacturing process:

1) *High h Region (Region highlighted by the dashed red line.):* In the low region, where the hatch distance *h* is relatively large, not all material is melted, leading to a reduction in density. This region is characterized by incomplete melting due to the significant spacing between scan paths.
2) *High Energy Region (Region highlighted by the dashed blue line.):* At high energy levels, depicted as an upward-sloping line with a slope of 1, small bubbles of evaporated material are formed. While this region exhibits a continuous increase in energy, the generation of evaporated material contributes to a bubble formation, causing a reduction in density, although not as abrupt as in the low region.
3) *Low Energy Region:* The left side of the graph represents scenarios where the hatch distance is sufficiently small to melt the entire material, but the power is insufficient for complete melting. This incomplete melting process, though less severe than in the low-distance region, results in a moderate reduction in density. Although points with a decrease in density are not apparent for this reason in Fig. 4 , they will be evident.
4) *High Density Region***:** The intermediate region, situated between the extremes of energy and just above High *h* Region, represents optimal conditions where the density is close to that of solid material without void spaces. This region is characterized by a balanced combination of energy, hatch distance, and power, resulting in an optimal density.

It's essential to note that the accuracy of these regions would be further pronounced with more precise measurements of absorptance, thermal conductivity, heat capacity, and density. Additionally, two outliers in the diagram may be attributed to the Gaussian distribution of power, a consideration not accounted for in the suggested one-dimensional scaling from a point-like laser spot to the actual Gaussian power distribution.

This analysis underscores the intricate interplay of process parameters and their impact on the final density of the Fe-6.5%Si alloy. Further refinement and experimentation, considering the Gaussian power distribution and precise material properties, would enhance the predictive capabilities of such diagrams.

B. *Density Variation in Fe-3%Si, Fe-6.7%Si, and Fe-6.9%Si Alloys*

Additionally, we investigated the density variations in Fe-3%Si, Fe-6.7%Si, and Fe-6.9%Si alloys based on data provided by [1], [6], and [3]. Figure Fig. 3 presents a comparative analysis of the density trends for these alloys, shedding light on the impact of silicon content on the final density. Similar to the previous figure, this diagram is scaled to the dimensions of the melt pool, calculated using the Méndez method as reported by Moda. As mentioned earlier, this type of diagram is highly dependent on a correct

choice of thermodynamic properties in addition to the scanning strategy. For this reason, the density of the author Andreiev is so close to the theoretical one; in particular, his work uses a scanning strategy that rotates 67 degrees between layers, which can enhance melting even though theenergy density is slightly lower than the one typically used. However, a decrease in density can be observed in the low-energy region.

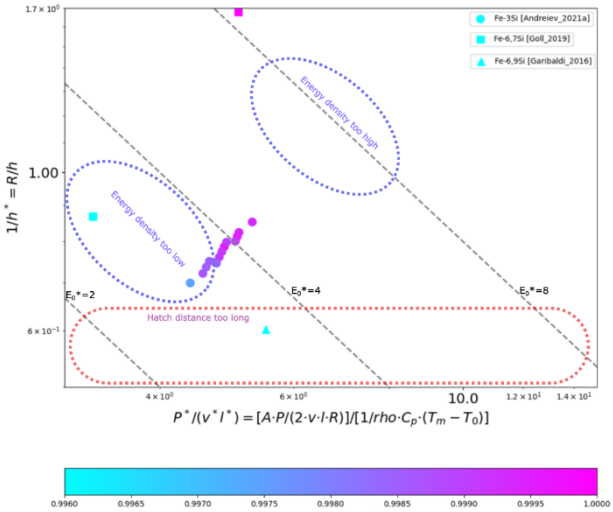


Figure 3: Standardized process diagram for Fe-3Si, Fe-6.7Si and Fe-6.9Si. Here the low energy region is highlighted by a blue dotted ellipse and encloses points with low density probably caused by incompletely molten material.

## IV. Conclusion and Perspectives

In conclusion, this study achieved several key outcomes. First, an enhanced normalized diagram was adapted to discern the impact of constructive parameters on the density of iron-silicon magnetic alloys. Second, stratified density regions were identified, facilitating the targeting of optimal construction points. Third, the construction of standardized diagrams is improved by considering the shape of the melt pool rather than solely relying on the laser spot radius.

These findings contribute to a nuanced understanding of the intricate relationship between process parameters and the density of magnetic materials. The adapted normalized diagram provides valuable insights into the regions where incomplete melting, bubble formation, insufficient power for melting, and optimal conditions occur. Utilizing this information allows for a more refined optimization of process parameters, influencing microstructure and, consequently, enhancing the efficiency of electric machines through tailored magnetic induction circuits.

## Acknowledgment

The authors acknowledge the financial support of the Hauts-de-France region in the frame of the "CONTRAT PLAN ÉTAT-RÉGION 2021-2027 EE 4.0" as well as the French National Research Agency (ANR) through the FALSTAFF project N° ANR-22-CE08-0029-01. The authors are also grateful to Roberval-UTC and ICB-LERMPS technical staff for their support.

## References

[1] Anatolii Andreiev, Kay-Peter Hoyer, Dimitri Dula, Florian Hengsbach, Olexandr Grydin, Yaroslav Frolov, and Mirko Schaper. Laser beam melting of functionally graded materials with application-adapted tailoring of magnetic and mechanical performance. Materials Science and Engineering: A, 822:141662, August 2021.

[2] Anatolii Andreiev, Kay-Peter Hoyer, Dimitri Dula, Florian Hengsbach, Michael Haase, Jan Gierse, Detmar Zimmer, Thomas Tröster,, and Mirko Schaper. Soft-magnetic behavior of laser beam melted fesi3 alloy with graded cross-section. Journal of Materials Processing Technology, 296:117183, October 2021.

[3] Michele Garibaldi, Ian Ashcroft, Marco Simonelli, and Richard Hague. Metallurgy of high-silicon steel parts produced using selective laser melting. Acta Materialia, 110:207–216, May 2016.

[4] M. Garibaldi, I. Ashcroft, N. Hillier, S.A.C. Harmon, and R. Hague. Relationship between laser energy input, microstructures and magnetic properties of selective laser melted fe-6.9 Materials Characterization, 143:144–151, September 2018. Metal Additive Manufacturing: Microstructures and Properties.

[5] M. Garibaldi, I. Ashcroft, J.N. Lemke, M. Simonelli, and R. Hague. Effect of annealing on the microstructure and magnetic properties of soft magnetic fe-si produced via laser additive manufacturing. Scripta Materialia, 142:121–125, 2018.

[6] D. Goll, D. Schuller, G. Martinek, T. Kunert, J. Schurr, C. Sinz, T. Schubert, T. Bernthaler, H. Riegel, and G. Schneider. Additive manufacturing of soft magnetic materials and components. Additive Manufacturing, 27:428–439, May 2019.

[7] D. Goll, J. Schurr, F. Trauter, J. Schanz, T. Bernthaler, H. Riegel, and G. Schneider. Additive manufacturing of soft and hard magnetic materials. Procedia CIRP, 94:248–253, 2020. 11th CIRP Conference on Photonic Technologies [LANE 2020].

[8] J.C. Ion, H.R. Shercliff, and M.F. Ashby. Diagrams for laser materials processing. Acta Metallurgica et Materialia, 40(7):1539–1551, July 1992.

[9] Bonuk Koo, Min-Sun Jang, Yeong Gyun Nam, Sangsun Yang, Jihun Yu, Yong Ho Park, and Jae Won Jeong. Structurally-layered soft magnetic fe-si components with surface insulation prepared by shell-shaping selective laser melting. Applied Surface Science, 553:149510, July 2021.

[10] Andreas Krings, Aldo Boglietti, Andrea Cavagnino, and Steve Sprague. Soft magnetic material status and trends in electric machines. IEEE Transactions on Industrial Electronics, 64(3):2405–2414, March 2017.

[11] Andreas Krings, Marco Cossale, Alberto Tenconi, Juliette Soulard, Andrea Cavagnino, and Aldo Boglietti. Magnetic materials used in electrical

machines: A comparison and selection guide for early machine design. IEEE Industry Applications Magazine, 23(6):21–28, November 2017.

[12] Patricio F. Mendez, Yi Lu, and Ying Wang. Scaling analysis of a moving point heat source in steady-state on a semi-infinite solid. Journal of Heat Transfer, 140(8), April 2018.

[13] Jyrki Miettinen. Calculation of solidification-related thermophysical properties for steels. Metallurgical and Materials Transactions B, 28(2):281–297, April 1997.

[14] Mattia Moda, Andrea Chiocca, Giuseppe Macoretta, Bernardo Monelli, and Leonardo Bertini. Technological implications of the rosenthal solution for a moving point heat source in steady state on a semi-infinite solid. Materials & Design, 223:110991, 07 2022.

[15] A. Plotkowski, J. Pries, F. List, P. Nandwana, B. Stump, K. Carver, and R.R. Dehoff. Influence of scan pattern and geometry on the microstructure and soft-magnetic performance of additively manufactured fe-si. Additive Manufacturing, 29:100781, October 2019.

[16] Tuomas Riipinen, Tomi Lindroos, Sini Metsä-Kortelainen, Janne Keränen, Juha Lagerbom, Aino Manninen, and Jenni Pippuri-Mäkeläinen. Mechanical and magnetic properties of fe-co-v alloy produced by selective laser melting. (Ltd,), 2018.

[17] Giulia Stornelli, Antonio Faba, Andrea Di Schino, Paolo Folgarait, Maria Rita Ridolfi, Ermanno Cardelli, and Roberto Montanari. Properties of additively manufactured electric steel powder cores with increased si content. Materials, 14(6):1489, March 2021.

[18] Meurig Thomas, Gavin J. Baxter, and Iain Todd. Normalised model-based processing diagrams for additive layer manufacture of engineering alloys. Acta Materialia, 108:26–35, April 2016.

[19] Meher Zaied, Alejandro Ospina-Vargas, Nicolas Buiron, Jérôme Favergeon, and Nour-Eddine Fenineche. Additive manufacturing of soft ferromagnetic fe 6.5%si annular cores: Process parameters, microstructure, and magnetic properties. IEEE Transactions on Magnetics, 58(11):1–9, 2022.